nature communications

Article

https://doi.org/10.1038/s41467-025-65588-0

Enabling ambient stability and quantum integration of organometallic magnonic ferrimagnets via atomic layer encapsulation

Received: 26 June 2025

Accepted: 16 October 2025

Published online: 26 November 2025

Check for updates

M. Iqbal Bakti Utama[1,10], Robert Claassen[2,10], Srishti Pal[3,10], Donley S. Cormode[2], Dmitry Lebedev[1,8], Subhajyoti Chaudhuri[4], Qin Xu[5], Hong Youl Park[1], Seok Daniel Namgung[1,9], George C. Schatz[4], Gregory D. Fuchs[3,6] ✉, Ezekiel Johnston-Halperin[2] ✉ & Mark C. Hersam[1,4,7] ✉

Magnons, the quanta of spin waves in magnetic materials, are promising for hybrid quantum systems by bridging electromagnetic and spin degrees of freedom. The organometallic ferrimagnet vanadium tetracyanoethylene ($V[TCNE]_x$, $x \approx 2$) is especially well-suited for quantum magnonics due to its low Gilbert damping and substrate versatility. However, its rapid chemical degradation in ambient conditions hinders practical applications. Incumbent encapsulation methods provide some protection, but are bulky, obscure intrinsic properties of $V[TCNE]_x$, introduce thermal stress at cryogenic temperatures, and complicate microwave device integration. Here, we demonstrate that ultrathin alumina films deposited via low-temperature atomic layer deposition effectively protect $V[TCNE]_x$ by preserving its magnetic and magnonic properties following ambient exposure. The sub-100 nm transparent films also enable advanced spectroscopy, magnetometry, and cavity magnonic measurements that reveal the intrinsic properties of $V[TCNE]_x$. This encapsulation strategy advances molecule-based quantum information science by providing a robust route toward scalable, monolithic integration in hybrid quantum technologies.

Organic molecular materials offer unparalleled synthetic tunability, which when paired with exceptional optoelectronic and magnetic properties, make them highly attractive for applications in energy conversion, display technologies, and information science[1,2]. In the rapidly advancing field of quantum information technology, molecular spin and magnetic materials have emerged as promising candidates for quantum bits and quantum sensing applications[3–8]. Among these, the room-temperature ferrimagnet[9] vanadium tetracyanoethylene ($V[TCNE]_x$ where $x \approx 2$) is the leading molecular material for magnonic interconnects[10], bridging disparate qubit modalities in hybrid quantum systems[11–16]. $V[TCNE]_x$ exhibits narrow ferromagnetic resonance (FMR) linewidth (~1 G peak-to-peak at 9.8 GHz and room

[1]Department of Materials Science and Engineering, Northwestern University, Evanston, IL, USA. [2]Department of Physics, The Ohio State University, Columbus, OH, USA. [3]School of Applied and Engineering Physics, Cornell University, Ithaca, NY, USA. [4]Department of Chemistry, Northwestern University, Evanston, IL, USA. [5]Department of Physics, Cornell University, Ithaca, NY, USA. [6]Kavli Institute at Cornell for Nanoscale Science, Cornell University, Ithaca, NY, USA. [7]Department of Electrical and Computer Engineering, Northwestern University, Evanston, IL, USA. [8]Present address: Department of Quantum Matter Physics, University of Geneva, Geneva, Switzerland. [9]Present address: School of Electrical and Electronics Engineering, Chung-Ang University, Seoul, Republic of Korea. [10]These authors contributed equally: M. Iqbal Bakti Utama, Robert Claassen, Srishti Pal. ✉e-mail: gdf9@cornell.edu; johnston-halperin.1@osu.edu; m-hersam@northwestern.edu

temperature)[17,18] and low Gilbert damping (as low as $\alpha = 4\times10^{-5}$ for unpatterned films)[19–22], comparable to that of industry-standard epitaxial yttrium iron garnet (YIG)[23]. Moreover, unlike YIG, V[TCNE]$_x$ offers the advantages of low-temperature processability (40 °C–60 °C) and the ability to be deposited on diverse substrates without epitaxial constraints[24,25].

Despite their remarkable properties, molecular spin and magnetic materials often face significant challenges due to rapid chemical degradation upon exposure to ambient conditions. This issue has spurred intensive efforts to develop strategies to improve their ambient stability so that their exceptional characteristics can be fully exploited in practical applications[26,27]. V[TCNE]$_x$ is particularly susceptible to chemical degradation, which implies that it quickly loses its magnetic properties upon contact with ambient air[9]. Existing encapsulation methods, such as ultraviolet-cured epoxy combined with solid capping materials like glass or sapphire coverslips[21,28,29], offer some protection to V[TCNE]$_x$. However, these techniques introduce notable limitations, particularly bulky millimeter-thick epoxy layers that constrain the design of microwave waveguide chips for magnonic addressability. Furthermore, epoxy-based encapsulation is not ideal for cryogenic conditions due to thermal stress that causes delamination (Supplementary Fig. 1), thus impeding measurements of the intrinsic properties of V[TCNE]$_x$ at low temperatures.

Here, we demonstrate that ultrathin alumina films, deposited via low-temperature atomic layer deposition (ALD), offer an effective encapsulation strategy for V[TCNE]$_x$. Alumina was selected for several reasons: (1) Chemical inertness of alumina, which provides a robust barrier against oxygen and moisture; (2) A purely thermal ALD process with low deposition temperature (30 °C–50 °C) without sacrificing low pinhole density, conformality, and overall film quality, all of which are essential for protecting V[TCNE]$_x$ while avoiding its thermal degradation; (3) Relatively low dielectric loss of alumina compared to other ALD grown insulating oxides, which is particularly advantageous in cavity magnonics, where minimizing dielectric loss is critical for preserving cavity quality factors and coherence.

With sub-100 nm thicknesses, these alumina films significantly enhance the ambient stability of the magnetic and magnonic properties of V[TCNE]$_x$ by several orders of magnitude while preserving access to intrinsic characteristics. The optical transparency of alumina, spanning from the deep-ultraviolet to the mid-infrared, enables detailed spectroscopic and magnetometric analyses, including measurement methods that have not previously been applied to this material. Additionally, the compatibility of ultrathin alumina with milli-Kelvin temperatures and repeated thermal cycling positions it as an ideal encapsulation material for quantum metrology. In this manner, this work advances molecule-based quantum information science and technology by enabling scalable, monolithic on-chip integration.

Results And Discussion

Preservation of magnetic and magnonic properties

Figure 1a illustrates the process of alumina growth via ALD, which involves sequential pulsing and purging of trimethyl aluminum (TMA) and water vapor precursors. To adapt the standard microelectronics ALD alumina process for encapsulating V[TCNE]$_x$, three key modifications were implemented. First, the V[TCNE]$_x$ sample is kept free from ambient air exposure preceding alumina deposition through the use of an ALD system integrated with an inert atmosphere glove box (see Methods)[31–33]. Second, the deposition temperature is lowered to prevent thermal degradation of V[TCNE]$_x$, which undergoes irreversible exothermic processes at 80 °C (refs. 24,34). Our optimized deposition procedure allows high-quality, layer-by-layer ALD alumina growth at substrate temperatures of 30 °C–50 °C (Supplementary Fig. 2)[35], significantly lower than the typical 150 °C–300 °C used in

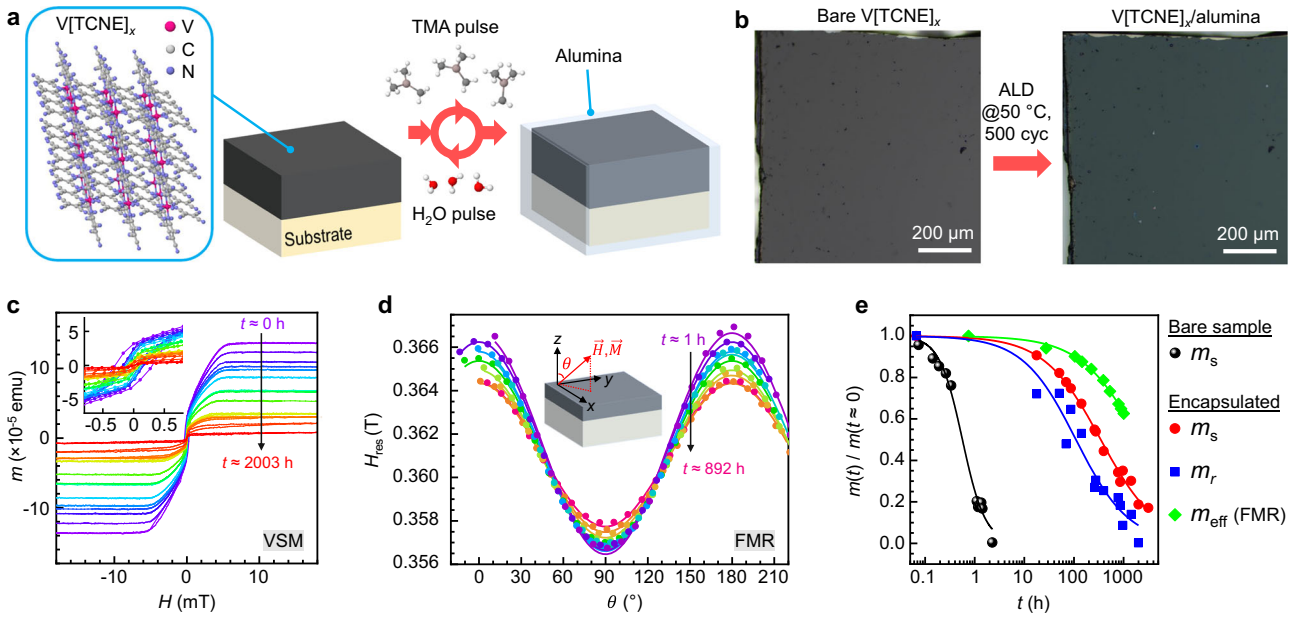

Fig. 1 | Preservation of magnetic and magnonic properties of V[TCNE]$_x$ with ultrathin alumina encapsulation. a Schematic of the ALD alumina deposition process (Atom colors: red, O; white, H; black, C; brown, Al). *Inset*: Molecular structure of V[TCNE]$_x$, consisting of a network of V^{2+} with octahedral coordination[30] bonded to TCNE molecules. **b** Representative optical micrographs of a V[TCNE]$_x$ sample before and after 500 cycles of alumina deposition at 50 °C. **c** Plot of m vs. H from in-plane VSM measurements of ALD alumina-encapsulated V[TCNE]$_x$ after various durations of ambient exposure (t). *Inset:* Zoom-in near $H = 0$, showing coercivity and remanent field in the hysteresis loop. **d** Angle dependence of H_{res} from cavity-FMR measurements of ALD alumina-encapsulated V[TCNE]$_x$ at different ambient exposure durations (t). *Inset*: Measurement schematic defining the angle θ. Data are fit with Eq. (1). **e** Time evolution of magnetic parameters (m_s, m_r, m_{eff}) for alumina-encapsulated V[TCNE]$_x$, normalized to values at t ≈ 0. The evolution of m_s for a bare sample is shown for comparison, demonstrating that alumina encapsulation enhances ambient stability by several orders of magnitude. The data are fit using an empirical function to aid visualization (Supplementary Fig. 12b, c).

microelectronics[36]. Third, to mitigate water-induced degradation, an initial seeding step of 10 TMA half-cycles is included to fully saturate the surface[31–33], thus minimizing direct contact of V[TCNE]$_x$ with water. Together, these adjustments result in conformal ALD alumina encapsulation of V[TCNE]$_x$ that can be employed on arbitrarily large substrates (Supplementary Fig. 2d, e).

In our experiments, V[TCNE]$_x$ films were deposited via chemical vapor deposition (CVD) with a thickness of approximately 300 nm – 1.3 µm, as confirmed by ellipsometry (Supplementary Fig. 3a) and atomic force microscopy (AFM). Figure 1b presents optical microscopy images of V[TCNE]$_x$ before and after encapsulation with alumina. No structural or morphological changes are observed, suggesting a highly conformal film. X-ray photoelectron spectroscopy (XPS) further reveals that the alumina film is nearly stoichiometric, with an Al:O atomic ratio of 1:1.57 (Supplementary Fig. 3c). AFM measurements confirm that the alumina film grows smoothly and conformally on V[TCNE]$_x$, with surface roughness values closely matching those of bare V[TCNE]$_x$ (i.e., 1.04 nm versus 1.21 nm surface roughness for ALD-encapsulated and bare V[TCNE]$_x$, respectively; Supplementary Fig. 4h, i). We further confirm that the ALD process does not disturb the chemical structure or magnetic properties of V[TCNE]$_x$ through Raman, magnetic, and XPS depth-profiling analyses (Supplementary Figs. 5-6), thereby demonstrating that the encapsulation is fully compatible with V[TCNE]$_x$ and that ALD alumina protects the pristine material rather than chemically altering the film.

Figure 1c presents vibrating sample magnetometry (VSM) measurements of alumina-encapsulated V[TCNE]$_x$ at $T = 300$ K. While bare V[TCNE]$_x$ loses all magnetic properties within 2 h of ambient exposure[28] (Supplementary Fig. 7b, c), V[TCNE]$_x$ encapsulated with ~50 nm thick ALD alumina (50 °C, 500 cycles) demonstrates significant enhancement in ambient stability (Fig. 1c), retaining measurable magnetic moment even after more than 2000 h of air exposure (also see Supplementary Fig. 7a). This performance surpasses prior encapsulation using parylene[37] and rivals the stability provided by ultraviolet-cured epoxy despite ALD-encapsulation being over 5000 times thinner.

Cavity FMR spectroscopy at the X-band was also performed in ambient conditions on a V[TCNE]$_x$ sample encapsulated with ~80 nm thick ALD alumina (34 °C, 800 cycles). The FMR spectra were collected as a function of the sample orientation relative to the applied magnetic field (θ) for different durations of ambient exposure (Supplementary Fig. 8). The resonance magnetic field (H_{res}) extracted from the spectra is shown in Fig. 1d. The effective field, H_{eff}, is defined as[22]:

$$H_{eff} = M_{eff} = M_s - H_k \tag{1}$$

where M_s represents the saturation magnetization and H_k denotes the crystal-field anisotropy. H_{eff} is extracted from the FMR spectra by fitting to the equation[38]:

$$\omega/\gamma = \sqrt{(H - H_{eff}\cos^2\theta)(H - H_{eff}\cos 2\theta)} \tag{2}$$

where ω is the resonance frequency and γ is the gyromagnetic ratio. Using Eq. (2), we extract H_{eff} from the angle-dependent cavity-FMR measurements as a function of ambient exposure duration. We note that the FMR anisotropy measurement is sensitive to the volume-normalized M_s and is not impacted by the removal of material such that the extracted H_{eff} is not directly affected if some fraction of the volume becomes non-magnetic upon degradation.

We plot the effective moment (m_{eff}) from FMR alongside the saturation moment (m_s, extracted from m versus H with wider magnetic field sweep in Supplementary Fig. 7a) and remanent field (m_r) from VSM measurements (Fig. 1c), normalized to their respective values at $t \approx 0$ (Fig. 1e). Broadband FMR measurements over the range of 2–30 GHz also revealed that the Gilbert damping of alumina-encapsulated V[TCNE]$_x$ remains unchanged after hundreds of hours of ambient exposure (Supplementary Fig. 9c-d, Supplementary Table 1). Overall, these magnetometry experiments consistently show that ALD encapsulation preserves the magnetic properties of V[TCNE]$_x$, even with sub-100 nm alumina thickness.

The success of the encapsulation strategy is limited by the surface cleanliness of the V[TCNE]$_x$ film. Point asperities on the surface of the V[TCNE]$_x$ film, such as crystallized microparticles or other debris, can create pinholes in the alumina layer, allowing oxygen or moisture to penetrate and degrade the underlying V[TCNE]$_x$ (Supplementary Fig. 10). These challenges can be mitigated by controlling the CVD growth conditions to reduce the formation of crystallized microparticle byproducts. Additionally, cleaning the V[TCNE]$_x$ film surface with PDMS stamping prior to ALD alumina deposition helps remove debris and ensure a conformal ALD encapsulation layer with minimal defects.

ALD alumina has been widely used for encapsulating various materials in organic electronics and optoelectronics (e.g., organic light-emitting diodes, perovskite solar cells) as demonstrated in prior reports[27]. However, ALD encapsulation is rarely discussed for magnetic materials, whether inorganic or organic. Even in the case of air-sensitive inorganic magnetic materials, the implementation of ALD encapsulation can be non-trivial. For instance, in antiferromagnetic van der Waals CrI_3, direct ALD deposition of alumina was shown to damage the material and alter its magnetic properties, requiring specialized procedures with organic seeding layers to prevent degradation[33].

Likewise, the feasibility of ALD encapsulation for preserving V[TCNE]$_x$ was far from obvious, which likely explains why this approach has remained unreported in the decades since the discovery of this material, despite the widespread use of ALD in other contexts. V[TCNE]$_x$ is highly chemically sensitive, and our work identifies the key modifications from the standard ALD process required to make the encapsulation viable. Thus, while ALD as a technique is well established, our study demonstrates its first successful application to an organic-based magnet, overcoming long-standing challenges that previously hindered its adoption. Additionally, these advances are not merely procedural but are essential for enabling the broad range of magnetic, magnonic, and optical characterization discussed below. In this manner, encapsulation is not simply a supporting step, but rather a central technical advance that unlocks new experimental access and fundamental insights into the intrinsic properties of V[TCNE]$_x$.

Optical and vibrational spectroscopy

The sub-100 nm thickness and optical transparency of ALD-deposited alumina allow detailed evaluation of the optical properties of V[TCNE]$_x$ under ambient conditions, particularly when grown on double-polished CaF_2, which is highly transparent from the deep-ultraviolet (DUV) (DUV, absorption onset at ~200 nm) to the mid-infrared (mid-IR) region. Figure 2a qualitatively demonstrates the preservation of the film color for alumina-encapsulated V[TCNE]$_x$ in ambient conditions. While bare V[TCNE]$_x$ undergoes oxidation and degradation, resulting in a transition to a more transparent color, the alumina-encapsulated sample retains its characteristic dark blue color. Quantitative optical characterization using UV-vis-NIR spectroscopy corroborates this observation (Fig. 2b). While the absorbance of bare V[TCNE]$_x$ rapidly decreases within the first 30 minutes of ambient exposure (Supplementary Fig. 11), the alumina-encapsulated sample exhibits minimal changes in absorbance over a period of 5 days (also see Supplementary Fig. 12a).

The absorbance spectrum of alumina-encapsulated V[TCNE]$_x$ closely aligns with electronic transitions measured using electron energy loss spectroscopy (EELS) in scanning transmission electron microscopy (STEM)[39]. The ultrathin alumina enhances the determination of electronic transitions in V[TCNE]$_x$ by providing a significantly

https://doi.org/10.1038/s41467-025-65588-0

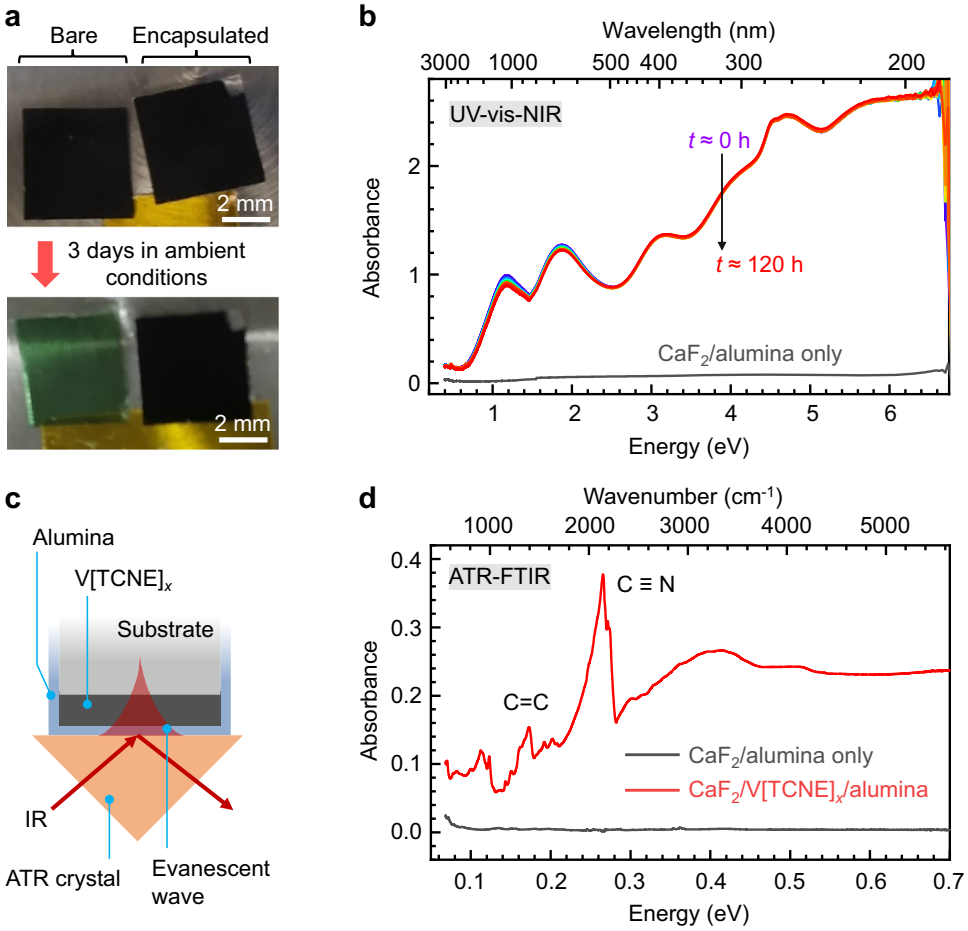

Fig. 2 | Optical and vibrational spectroscopy of V[TCNE]$_x$. The sub-100 nm thickness and optical transparency of ALD alumina, spanning from DUV to mid-IR, enable detailed spectroscopic studies of V[TCNE]$_x$. **a** Photographs of bare (left) and alumina-encapsulated V[TCNE]$_x$ samples (right) before and after 3 days of ambient exposure. The encapsulated sample retains the characteristic dark blue color of V[TCNE]$_x$, while the bare sample shows visible degradation. **b** UV-vis-NIR absorbance spectra of alumina-encapsulated V[TCNE]$_x$ on a CaF_2 substrate as a function of exposure time to ambient conditions, demonstrating minimal changes in absorbance over time. **c** Schematic of the ATR-FTIR measurement for alumina-encapsulated V[TCNE]$_x$. The ultrathin alumina layer and IR-transparent CaF_2 substrate allow for artifact-free measurements in ATR mode. **d** ATR-FTIR spectra of alumina-encapsulated V[TCNE]$_x$ on a CaF_2 substrate and a blank CaF_2/alumina substrate, highlighting the vibrational features of V[TCNE]$_x$.

higher signal-to-noise ratio compared to STEM-based EELS. Moreover, this method avoids the risk of radiation damage caused by electron beams, and the spectra can be analyzed using a blank CaF_2 as a background reference, eliminating the need for additional fitting procedures to remove the zero-loss EELS peak. The absorbance spectrum further reveals an onset in the IR region, attributed to a transition between spin-opposite, dipole-forbidden bands. Using the Tauc relation (Supplementary Fig. 13a), the bandgap is determined to be 0.586 eV, consistent with previous measurements from electrical transport measurements[40] and EELS[39]. Moreover, Gaussian fitting of the absorbance spectrum identifies peaks that correspond to electronic transitions with energies at 1.131, 1.865, 3.234, 3.953, and 4.555 eV (Supplementary Fig. 13b, c) that are consistent with previously reported EELS results[39]. The improved accuracy of these values, enabled by the ultrathin ALD alumina encapsulation, provides valuable input for first-principles calculations aimed at elucidating the underlying physics of these transitions (Supplementary Figs. 14-15). Specifically, our first-principles calculations revealed that the primary absorption features in the 0 – 2 eV range show metal-to-neighboring-ligand electronic transitions, the 3–4 eV range show ligand-to-ligand electronic transitions, and the >4 eV range show metal-to-non-neighboring-ligand electronic transitions (Supplementary Fig. 15).

Ultrathin alumina encapsulation layers facilitate additional spectroscopy characterization in ambient conditions that are not feasible with incumbent encapsulation methods. For example, Fourier transform infrared (FTIR) spectroscopy can be performed in the attenuated total reflection (ATR) mode. ATR-FTIR under ambient conditions has not previously been reported for V[TCNE]$_x$ because this method relies on the evanescent wave from the ATR crystal with a limited penetration depth of 2–5 µm (Fig. 2c), which requires sub-micron thick encapsulation layers with high infrared transparency. Unlike thick epoxy or bulk sapphire encapsulation, ALD alumina encapsulation is ultrathin and introduces minimal infrared background (Supplementary Fig. 16a-b). When combined with a CaF_2 substrate, ultrathin alumina encapsulation allows ATR-FTIR to be performed on V[TCNE]$_x$ without artifacts, thereby providing insight into vibrational properties. In particular, Fig. 2d presents the FTIR spectrum of alumina-encapsulated V[TCNE]$_x$ measured in ATR mode, compared with the spectrum of a CaF_2 substrate without V[TCNE]$_x$. The prominent feature at ~2131 cm^{-1} is attributed to C ≡ N vibrations, consistent with previous studies[9,28]. Additionally, the FTIR spectral region below 2000 cm^{-1} for V[TCNE]$_x$ (Supplementary Fig. 16c) is revealed with high signal-to-noise ratio. Based on previous Raman scattering results, we assign the feature centered at ~1374 cm^{-1} to C = C vibrational modes[20].

As a complementary measurement, Raman spectroscopy was also performed on the V[TCNE]$_x$ samples (Supplementary Fig. 5a-b, 17a-b). The Raman spectra of alumina-encapsulated V[TCNE]$_x$ are nearly identical to those of bare V[TCNE]$_x$, indicating that the ALD alumina deposition process does not alter the vibrational features or chemical stoichiometry of V[TCNE]$_x$. Additionally, alumina encapsulation enhances the robustness of V[TCNE]$_x$ against laser-induced degradation[20] (Supplementary Fig. 17c-f), which is likely due to the high thermal conductivity of alumina that quickly dissipates the localized heating from the excitation laser away from the irradiation spot.

Magnetic force microscopy

The ultrathin nature of ALD alumina further enables characterization of V[TCNE]$_x$ using surface-sensitive probes. One such technique is magnetic force microscopy (MFM), which uses an AFM probe tip coated with a ferromagnetically polarized film. Despite the four decades of research on metal-TCNE magnetic materials, previous work has not yet successfully performed spatially-resolved magnetometry on V[TCNE]$_x$ or other vanadium-based molecular magnets. The only previously reported MFM study was conducted on Cu[TCNE]$_x$ without any special treatment or encapsulation[41], despite the air sensitivity of the material. Two primary challenges have likely limited the application of MFM in this field. First, the ambient sensitivity of V[TCNE]$_x$ and the need for thick epoxy encapsulation have prevented MFM from being conducted in ambient conditions. Second, MFM requires features capable of generating sufficient spatial contrast in the MFM phase image. Directly observing magnetic domains in V[TCNE]$_x$ is challenging due to its small coercivity (<20 Oe) and low saturation field (<100 Oe), which can be influenced by the stray fields from the ferromagnetic MFM tip. Furthermore, lithographic patterning of V[TCNE]$_x$ has only recently been reported[19], limiting its integration with spatially resolved techniques.

To generate spatial contrast of the magnetic properties of V[TCNE]$_x$, we leveraged its chemical degradation behavior, which results in a clear boundary between degraded and pristine V[TCNE]$_x$ near the edge of the sample[20] (see Supplementary Fig. 10b–d). In alumina-encapsulated samples, this edge degradation becomes apparent after several weeks of ambient exposure, progressively reducing the magnetic moment over time until the sample becomes fully diamagnetic (Fig. 1c–e). Figure 3a shows this process, with a discrete border separating distinctly colored pristine and degraded regions, as schematically illustrated in Fig. 3b. The AFM height image of the sample (Fig. 3c) reveals no obvious topographic changes across the border, while the corresponding MFM image (Fig. 3d) shows clear phase contrast. The histogram of MFM phase contrast (Fig. 3e) further quantifies the differences between magnetic pristine V[TCNE]$_x$ region and degraded, diamagnetic V[TCNE]$_x$. Importantly, alumina encapsulation plays a critical role in enabling these MFM measurements. By coating both the pristine and degraded areas, the alumina encapsulation minimizes issues resulting from short-range van der Waals interactions, differences in mechanical stiffness, and surface charging, all of which could otherwise contribute to the MFM phase image and obscure the contribution from magnetic properties (Supplementary Fig. 18).

Milli-Kelvin Cavity Magnonics

The low temperature compatibility of ALD alumina, compared to epoxy (Supplementary Fig. 1), facilitates cavity magnonic experiments of V[TCNE]$_x$ at cryogenic temperatures. Specifically, we integrated a lumped element superconducting resonator[42] with lithography-assisted deposition of V[TCNE]$_x$ (see Methods). The oscillating current concentrated on the inductor wire of the resonator generates the Oersted field that excites the magnon modes of the V[TCNE]$_x$ strip. The response of this coupled photon-magnon system is then detected through the microwave feedline to which the resonator is coupled capacitively. In order to protect the V[TCNE]$_x$ spins patterned on the resonator inductor, ALD alumina deposition (34 °C, 550 cycles) was performed using a PDMS-masking procedure (Supplementary Fig. 19) to achieve selective-area deposition, thereby limiting the alumina layer to the region surrounding the V[TCNE] strip. This approach effectively minimizes the reduction of resonator Q-factor (Supplementary Fig. 20 and Table 2). A fully fabricated device with alumina encapsulation is shown in Fig. 4a–c[42].

The resulting device was first measured at zero magnetic field and a temperature $T = 0.44$ K, which is a regime where the resonator and magnon modes are strongly detuned. The $|S_{21}|$ spectrum shown in Fig. 4d was fit (Eq. (5) in Methods section) to yield a loaded $Q_l = 10{,}104$, coupling $|Q_c| = 17{,}094$, internal $Q_i = 24{,}705$, and resonance frequency $\omega_r/2\pi = 3.9758$ GHz. These Q-factors surpass those achieved in previous cavity magnonic experiments of V[TCNE]$_x$ with epoxy encapsulation[42], highlighting the advantage of the small form factor provided by the ALD alumina encapsulation.

Subsequently, the external magnetic field was tuned closer to the resonance between the fundamental mode of the resonator and the $k = 0$ uniform magnon Kittel mode of V[TCNE]$_x$, creating a hybrid excitation of cavity microwave photons and V[TCNE]$_x$ magnons. These conditions result in the avoided level crossing in the microwave transmission spectrum as shown in Fig. 4e, thus allowing direct study

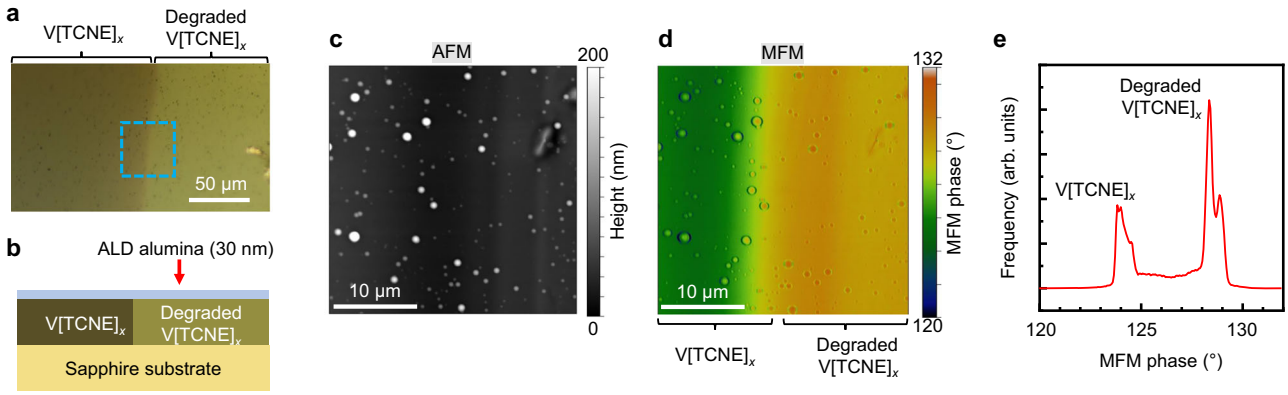

Fig. 3 | Magnetic force microscopy of V[TCNE]$_x$. **a** Optical microscope image of an alumina-encapsulated V[TCNE]$_x$ sample following 4 weeks of ambient exposure. Partial degradation is visible, with a discolored front advancing from the edge of the chip. **b** Schematic cross-section of the sample in (**a**). **c** AFM height image from the region marked by the dashed blue square in (**a**). **d** MFM image of the same region in (**c**), revealing distinct phase contrast between the pristine and degraded V[TCNE]$_x$ regions. **e** Histogram of MFM phase data from (**d**), quantifying the MFM phase differences between the two regions.

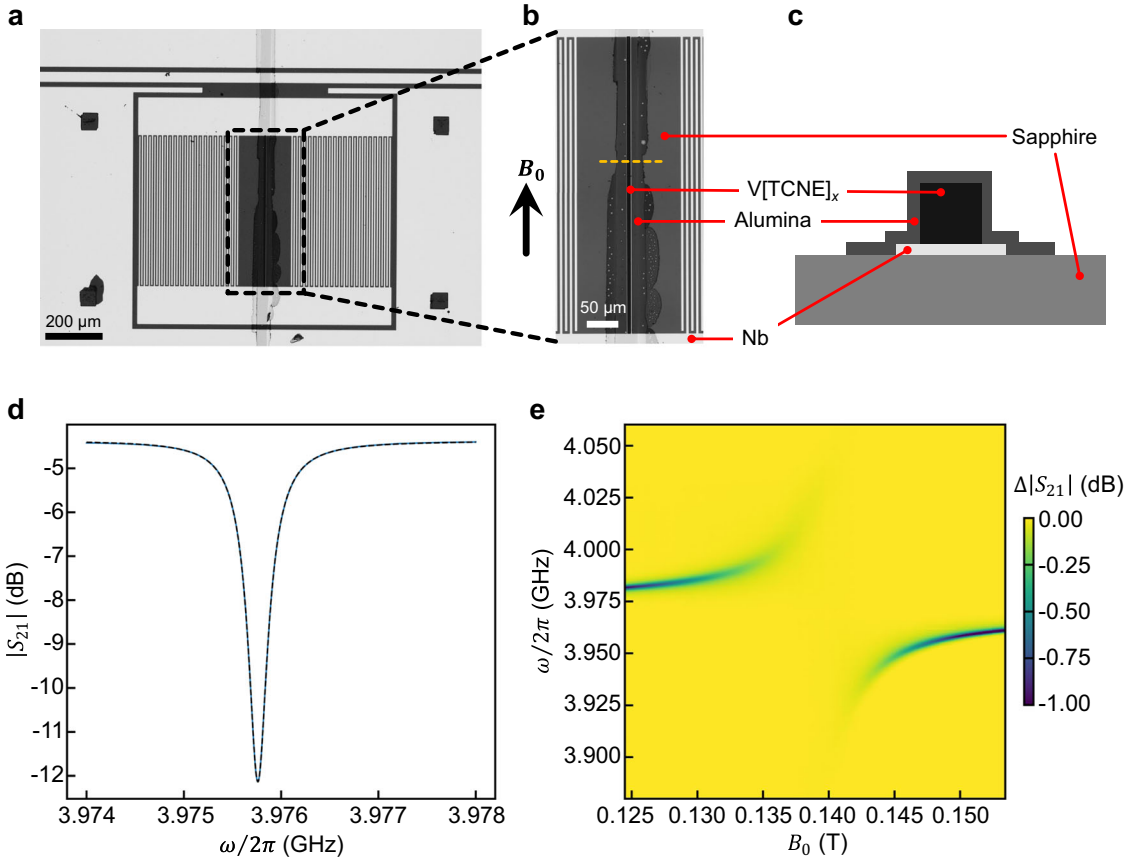

Fig. 4 | Coupling of microwave photons and V[TCNE]$_x$ magnons in a superconducting resonator. a Optical microscopy image of a superconducting resonator integrated with patterned V[TCNE]$_x$ and PDMS-masked alumina deposition. **b** Magnified optical microscopy image of the region marked with the black dashed rectangle in (**a**). **c** Cross-sectional schematic of the device along the yellow dashed line in (**b**). **d** Fitted (black dashed line) microwave transmission spectrum (blue curve) at zero static magnetic field and temperature = 0.44 K. **e** 2D colormap of $\Delta|S_{21}|$ as a function of static magnetic field and microwave frequency at 0.44 K, displaying an avoided level crossing between the microwave photon mode and the magnon Kittel mode.

of photon-magnon coupling. The eigenfrequencies of the coupled photon-magnon system are described by[11]:

$$\omega_{\pm} = \omega_r + \Delta/2 \pm \sqrt{\Delta^2 + 4g^2/2} \tag{3}$$

where $\Delta = \omega_m(B_0) - \omega_r$ represents the detuning, with the magnon frequency given by $\omega_m(B_0) = \gamma\sqrt{B_0(B_0 + \mu_0 M_{\mathrm{eff}})}$. B_0 is the in-plane static magnetic field applied parallel to the inductor wire (Fig. 4b), and M_{eff} is the effective magnetization as defined earlier (Eq. (1)). M_{eff} is influenced by the uniaxial anisotropy field (H_k) of the V[TCNE]$_x$ microstructure. Fitting the spectrum using Eq. (3) (Supplementary Fig. 20) yields $\mu_0 M_{\mathrm{eff}} = 3.311(7)$ mT, which is over an order of magnitude lower than previous reports based on epoxy encapsulation[42]. Given that V[TCNE]$_x$ typically exhibits low saturation magnetization ($\mu_0 M_s \sim 10$ mT)[19,22,39], the M_{eff} in previous epoxy-encapsulated samples was likely dominated by the H_k term, which is driven by the significant strain from differential thermal expansion[42]. In other words, the use of ultrathin alumina encapsulation has enabled the observation of photon-magnon hybridization with minimal influence of strain-induced anisotropy, which not only provides a more intrinsic measure of photon-magnon coupling but also facilitates reliable achievement of the resonance condition.

Finally, we show that the microwave resonator device with alumina encapsulation is compatible with thermal cycling (Supplementary Fig. 22a–c), which is a significant advantage over epoxy encapsulation. After the first cooling cycle from room temperature to 0.44 K, the sample was warmed back to room temperature, and without breaking the vacuum, subsequently cooled again to 0.44 K. The sample was then warmed up to room temperature and vented to ambient conditions for collection, where the sample was confirmed to remain intact (Supplementary Fig. 22c). During the second cooling cycle, the V[TCNE]$_x$ device again exhibited the same avoided level crossing behavior observed during the first cycle, confirming its robustness to thermal cycling. The reliable and reproducible attainment of the photon-magnon resonance condition following repeated thermal cycling is a critical step towards achieving quantum transduction in hybrid superconducting-magnonic quantum technologies.

Discussion

We have demonstrated that ultrathin alumina encapsulation via low-temperature ALD effectively preserves the magnetic, magnonic, and optical spectroscopic properties of V[TCNE]$_x$ following ambient exposure and processing. Beyond enhancing stability under ambient conditions, alumina encapsulation facilitates entirely new characterization or previously uncommon characterization approaches for V[TCNE]$_x$. The combination of sub-100 nm thickness and optical transparency ranging from deep-UV to mid-IR wavelengths enables diverse characterization of V[TCNE]$_x$ and provides insight into the

intrinsic properties of this material. Specifically, the encapsulation strategy has led to three key advances: (1) Observation of intrinsic photon-magnon coupling at cryogenic temperatures with minimal strain-induced anisotropy and the possibility for repeated thermal cycling; (2) Spectroscopic access to optical transitions and vibrational modes that clarified the nature of electronic transitions; (3) Spatially resolved magnetometry of $V[TCNE]_x$, enabling MFM imaging under ambient conditions. This capability has not previously been achieved for this class of materials and opens new pathways for exploring the micromagnetics of $V[TCNE]_x$ and organic magnets in general.

Alumina encapsulation of $V[TCNE]_x$ also provides a versatile platform for advanced quantum applications. For instance, the ultra-thin nature of alumina encapsulation provides significant flexibility for integrating $V[TCNE]_x$ with superconducting microwave circuits and waveguides, overcoming constraints imposed by traditional bulky encapsulation layers. Moreover, ALD encapsulation holds promise for reliably achieving magnon-spin transduction between $V[TCNE]_x$ and externally deposited molecular or solid-state spin systems, leveraging alumina as a precisely tunable spacer layer. Since the ALD encapsulation method described here is expected to be compatible with other emerging molecular magnonic materials, it will accelerate ongoing efforts to incorporate molecular qubits and transduction elements in diverse quantum information technologies.

Methods

CVD synthesis of $V[TCNE]_x$ thin films and patterned samples

Preparation of unpatterned thin films. The $V[TCNE]_x$ films were synthesized by CVD at the Ohio State University on sapphire wafers (University Wafer, 100 µm thick, double-side polished) or CaF_2 substrates (Crystran, 13 mm diameter and 1 mm thick optically-polished UV grade) following an established procedure[43]. Prior to synthesis, all substrates were thoroughly cleaned with a solvent chain of acetone, methanol, isopropanol, and deionized water (2×) and blown dry with N_2. This solvent cleaning was followed by a 10 min UV/ozone clean in a UVOCS T10× 10/OES to remove residual organic contaminants. Immediately preceding deposition, the sapphire substrates were baked at 110 °C in a N_2 glovebox to remove any moisture adsorbed onto the surface.

Preparation of patterned resonator samples. For $V[TCNE]_x$ deposition on patterned resonator samples, an individual resonator chip was spin-coated with a 495 PMMA A4/MMA (8.5) MAA EL11 resist bilayer and then exposed using electron-beam lithography to pattern a bar (6 µm wide and 600 µm long) centered on the inductor wire (10 µm wide and 600 µm long). The exposed chip was then developed and baked, followed by deposition of a 3 nm thick capping layer of Al, which was allowed to oxidize in air, forming Al_2O_3 to prevent outgassing of the resist during CVD deposition. The chip was then transferred into a nitrogen-purged glovebox for CVD deposition (at ≈ 45 °C) of a 300 nm thick $V[TCNE]_x$ film. Finally, liftoff was performed using dichloromethane. ALD alumina deposition (34 °C for 550 cycles) was then performed using the PDMS pre-masking (Supplementary Fig. 19) to allow the alumina deposition to be only on a limited area on the resonator surrounding the $V[TCNE]_x$ and inductor wire to minimize microwave loss. Optical microscopy images of the completed sample are shown in Fig. 4a, b.

In both cases, the $V[TCNE]_x$ films were deposited in a custom CVD reactor inside a N_2 glovebox (O_2 <1 ppm, H_2O <1 ppm). Prior to every growth, the quality of the atmosphere of the glovebox was verified with the colorimetric indicator, titanium metallocene. The pressure inside the CVD reactor for all growths was approximately -745 Torr relative to atmospheric pressure, with the temperature of the TCNE precursor, $V(CO)_6$ precursor, and growth substrate held at 60 °C, 9 °C, and 45 °C, respectively. Following $V[TCNE]_x$ film deposition, the samples were wrapped in Teflon and packed with quartz wool inside quartz tubes that were flame-sealed under vacuum, after which they were sent to Northwestern University for ALD alumina encapsulation. To minimize sample degradation during transit, the ampoules were transported cold in containers filled with dry ice.

ALD alumina deposition

Prior to ALD alumina deposition, as-grown $V[TCNE]_x$ samples were cleaned to remove large dust particles, debris, and shards by repeatedly pressing the top surface with a pad of PDMS (Supplementary Fig. 10f). These contaminants may originate as byproducts of the $V[TCNE]_x$ synthesis, from the substrate dicing process, or from adventitious contamination during handling and shipment. This cleaning step ensures a smoother surface for ALD deposition, resulting in a conformal alumina film with minimal pinhole density, which in turn enhances the durability and shelf life of the encapsulated $V[TCNE]_x$ sample.

ALD alumina was deposited using an Anric AT 410 reactor with TMA (Oakwood Chemical) and water vapor as the precursors. The reactor chamber entrance was connected to a nitrogen glovebox (LC Tech, O_2 and H_2O <1 ppm) to ensure that the sample was loaded without exposure to ambient air. The ALD process consisted of two stages: (1) an initial seeding phase with ten half-cycles of only TMA pulses to saturate the $V[TCNE]_x$ surface and minimize direct water exposure; (2) full ALD cycles alternating TMA and water vapor. ALD deposition was conducted at substrate temperatures of 30 °C–50 °C with a 60 s purging time after each TMA and water vapor pulse (Supplementary Fig. 2b). This process results in an alumina growth rate of approximately 1 Å/cycle (Supplementary Figs. 2f, 4c, d, 4f, g). Unless otherwise specified, the data presented in this work are based on alumina deposition at 50 °C for 500 cycles.

For patterned ALD growth, a soft PDMS mask was used to cover specific portions of the sample. The PDMS pad was aligned using a transfer stage and served as a mask during ALD alumina deposition (Supplementary Fig. 4a). After completing the deposition process, the PDMS mask was carefully peeled off using tweezers.

Characterization

AFM and MFM. AFM imaging was conducted using an Asylum Cypher S instrument in tapping mode with NCHR-W (NanoWorld) probes, operated at a scan rate of 0.5 Hz. MFM measurements were performed on the same AFM system using PPP-MFMR (Nanosensors) probes, which were magnetized with a NdFeB permanent magnet. MFM measurements were performed in dual-pass mode to ensure high sensitivity. Supplementary Fig. 18 confirms that the observed phase contrast in MFM arises from magnetic interactions between the tip and the $V[TCNE]_x$ film. All AFM and MFM data are processed with Gwyddion 2.6.2 software.

X-ray photoelectron spectroscopy. XPS measurements were conducted under high vacuum (pressure $<3 \times 10^{-7}$ mbar) using a Thermo Scientific Nexsa G2 XPS system in charge compensation mode with a nominal X-ray spot size of 400 µm. For the data in Supplementary Fig. 3, the survey spectrum was collected with an analyzer pass energy of 150.0 eV, a dwell time of 50 ms, and a step size of 1.00 eV. Core level spectra were acquired with an analyzer pass energy of 50.0 eV, dwell time of 50 ms, and step size of 0.02 eV. Before the measurements shown in Supplementary Fig. 3b-c, a brief ion beam etching step was performed to descum the sample surface. The XPS spectra were analyzed using Avantage 6.6.0. software and fit with a Smart background. All binding energy levels were calibrated to the adventitious carbon 1 *s* level at 284.8 eV.

To probe the impact of ALD alumina deposition near the alumina/$V[TCNE]_x$ interface at the nanometer scale (Supplementary Fig. 6), we performed XPS measurements on bare and alumina-encapsulated samples from the same $V[TCNE]_x$ chip. Both samples were transported

in low vacuum from a N_2 glove box to the load-lock of the XPS system using a transfer vessel (Thermo Scientific, 831-57-100-2). To allow XPS to probe $V[TCNE]_x$ layer underneath the alumina film, we take advantage of the finite penetration depth of XPS by depositing only a very thin layer of alumina (~0.6 nm from six full cycles at 35 °C) on the sample. Core level spectra in Supplementary Fig. 6 were acquired with an analyzer step size of 0.1 eV. The depth profiling was performed using cluster Ar_{500}^+ ion (8000 eV, 100 s etch time per cycle) due to its weaker penetration damage to prevent altering the chemical state of $V[TCNE]_x$.

VSM and CPW-based broadband FMR. VSM and broadband FMR with a coplanar waveguide (CPW) were performed in a Dynacool PPMS (Quantum Design). For all VSM and broadband FMR measurements, the applied magnetic field was oriented in-plane to the sample. The samples are mounted on the sample holder (quartz paddle for VSM and in-plane CPW for broadband FMR) using Kapton tape. Prior to these measurements, the sample was purged with helium gas, and the PPMS chamber was pumped down at $T = 300$ K to a pressure of approximately 32–37 Torr for VSM and 7–9 Torr for broadband FMR.

To confirm that magnetic behavior of $V[TCNE]_x$ is unaffected by the ALD process (Supplementary Fig. 5), we conducted a paired experiment by splitting a single chip into two pieces: one left without alumina deposition but sealed with UV epoxy (Ossila E132) to prevent degradation during transfer between N_2 glove box and PPMS) and the other encapsulated with ALD alumina (300 cycles, 37 °C). Magnetization (M) was obtained by normalizing the measured moment by sample volume, with the area measured by ImageJ from the micrograph of the samples and film thickness determined by AFM. The temperature dependence was performed between 1.8 and 400 K with a with a heating rate of 1.5 K/min following zero-field cooling. Saturation magnetization (M_s) vs. T between 10–250 K are fitted well ($R^2 > 0.995$) using the Bloch's spin wave model[44]:

$$M_s(T) = M_s(T = 0\text{K})\left(1 - \left(T/T_C^*\right)^{3/2}\right) \quad (4)$$

where we obtained that the extrapolated critical temperature T_c^* of ~580 K, which reflects the magnetic ordering strength, remains practically unchanged before and after ALD alumina deposition. These results confirm that the ALD encapsulation process does not alter the magnetic properties of $V[TCNE]_x$.

Broadband FMR measurements were performed using a CryoFMR-40 spectrometer (NanoOsc Instrument). FMR spectra were measured over the frequency range of 2–30 GHz, with a modulation field of 0.005 (equivalent to ~0.2 Oe peak-to-peak) and field step size of 0.3 Oe. The resonance field (H_{res}) and FMR linewidth (ΔH) values (Supplementary Fig. 9) were extracted by fitting the FMR spectra with a single Lorentzian function. The Gilbert damping (α) and inhomogenous broadening (ΔH_0) were determined using the linear fitting of $\Delta H = \frac{2\alpha}{\gamma}(2\pi f) + \Delta H_0$. The calculated values are summarized in Supplementary Table 1 for a $V[TCNE]_x$ sample under three different conditions: (1) as-deposited with ALD alumina and exposed to ambient air only during the mounting of the waveguide; (2) after one cooling cycle from $T = 300$ K to $T = 2.5$ K and back to $T = 300$ K; (3) after $t = 508.25$ hours (~21 days) of ambient exposure. All broadband FMR data are analyzed with NanoOsc PhaseFMR 2.8.0.2 software.

For time-evolution measurements of VSM (Fig. 1c) and CPW-based broadband FMR (Supplementary Fig. 9c–f), the sample was stored in a cabinet at ambient conditions with minimal exposure to ambient lighting. The room temperature and humidity during storage fluctuated between 20 °C–28 °C and 34–37%, respectively, throughout the duration of the experiment. The quoted durations of ambient exposure in the time-evolution plots exclude the time when the sample was under vacuum inside the PPMS.

Cavity FMR. FMR measurements were performed in an X-band (9.8 GHz) Bruker Elexsys E500 CW electron paramagnetic resonance (EPR) spectrometer. The frequency of the microwave source was tuned to match the resonant frequency of the cavity prior to each scan to ensure optimal cavity tuning through the series of measurements. All scans were performed with a 0.3 G modulation amplitude at 100 kHz modulation frequency. The scans were performed at the lowest possible microwave power (0.2 μW) to avoid sample heating and nonlinear effects that would otherwise distort the FMR line shape. The $V[TCNE]_x$ films deposited onto sapphire were mounted on a custom Macor ceramic sample holder with negligible background and loaded into quartz EPR tubes that were sealed inside a nitrogen glovebox. Samples were rotated in 10° increments to determine the angular dependence of the resonance condition.

Optical spectroscopy measurements. UV-vis-NIR absorbance spectra were measured under ambient conditions using an Agilent Cary 5000 UV-vis-NIR spectrophotometer. Data were collected at 2.0 nm with an averaging time of 0.1 s per point. Alumina-encapsulated samples were measured across the range of 3100–175 nm (Fig. 2b), while bare samples (Supplementary Fig. 11) were measured over a shorter range of 800–200 nm to reduce the measurement time for each single spectrum, as the absorbance continuously changes during the measurement process.

Fourier transform infrared (FTIR) spectroscopy was performed in attenuated total reflectance (ATR) mode in a Nexus 870 spectrometer (Thermo Nicolet) with 64 scans per measurement. Ellipsometry measurements were conducted using a J.A. Woollam M2000U Spectroscopic Ellipsometer.

Confocal Raman spectroscopy at room temperature was performed using a Horiba XploRA Plus system. Unpolarized spectra were collected in backscattering configuration using a 532 nm laser excitation and a 1200 gr/mm grating. A long working distance objective (Olympus LMPlanFLN x50, 0.50 NA) was used to focus the laser. The sample was mounted on a Linkam microscopy stage (HFS350EV-PB4) inside a nitrogen glove box, and the sealed stage was continuously pumped down to maintain an inert environment during measurements. The use of inert environment helps to mitigate complications from oxidation, and as such the observed changes in Raman spectra upon laser irradiation (Supplementary Fig. 17c, d) are likely to have originated from laser-induced degradation. Data in Supplementary Fig. 5a,b are collected with an excitation through a 0.1% neutral density filter, which was measured to have ~36.4 W output power after the objective, with 30 s acquisition time per spectrum, and the encapsulated sample was deposited with ALD alumina at 37 °C over 300 cycles. Data in Supplementary Fig. 17 are collected through a 1% neutral density filter, which has ~560 μW output power after the objective, and the encapsulated sample was deposited with ALD alumina at 50 °C over 500 cycles.

Microwave resonator fabrication and measurements

The superconducting LC resonators were fabricated by sputtering 50 nm of Nb (superconducting critical temperature $T_c = 8.8$ K) on a MOS-cleaned sapphire substrate. The sputtered wafer was then spin-coated with S1813/LOR3A photoresist bilayer, exposed in 5X g-line stepper, and developed with AZ 726MIF developer. The developed resist was descummed, and the Nb was etched using reactive ion etching before stripping the photoresist using Microposit Remover 1165.

Following $V[TCNE]_x$ deposition and ALD encapsulation on the resonator chip, the cavity magnonic experiments were performed inside a Bluefors LD250 He-3 cryostat at its base temperature of 0.44 K. The microwave transmission was measured using a vector network analyzer (VNA) with −76 dBm of microwave power at the sample, which is far below the nonlinear power level of the resonator.

The $\Delta|S_{21}|$ parameter of the device in the strongly detuned regime (Fig. 4d) was fit with the following equation[45]:

$$|S_{21}(\omega)| = \left| a \times \left(1 - \frac{(Q_l/|Q_c|)e^{i\phi}}{1 + 2iQ_l(\omega/\omega_{res} - 1)}\right)\right| \quad (5)$$

where a is the attenuation coefficient, $\omega_{res} \approx \omega_r$ is the resonator frequency, and Q_l is the loaded quality-factor. The coupling quality factor $|Q_c|$ represents the loss of resonator photons to the microwave waveguide. ϕ represents the phase introduced due to impedance mismatch. The Q factors for bare resonator, alumina-encapsulated bare resonator without $V[TCNE]_x$, and resonator with alumina-encapsulated $V[TCNE]_x$ are provided in Supplementary Table 2.

Calculation of the excited state spectra

To obtain the UV-vis-NIR spectrum of $V[TCNE]_x$, cluster models of $V[TCNE]_2$ were built based on the structure reported by Trout et al. [39], and TDDFT calculations were performed at the PBE/Def2-SVP level in Orca 5.0. To compare with the UV-vis-NIR measurements (Supplementary Fig. 13b), the calculated spectra were convoluted with a Gaussian with FWHM of 0.5 eV. Three primary peaks are observed in the 1–4 eV range in both measurement and computation. The lower energy transitions show either metal-to-ligand, ligand-to-metal, or ligand-to-ligand charge transfer character. The calculated spectra and transitions corresponding to the highest oscillator strength excitations are shown in Supplementary Fig. 14b–e. The theoretical and experimental results show a high degree of agreement.

Data availability

The data supporting the findings of this study can be found at https://figshare.com/s/e34d150e7358d1dd7795, and are also available from the corresponding authors.

References

1. Fu, Y. et al. Metal halide perovskite nanostructures for optoelectronic applications and the study of physical properties. *Nat. Rev. Mater.* **4**, 169–188 (2019).
2. Forrest, S. R. & Thompson, M. E. Introduction: organic electronics and optoelectronics. *Chem. Rev.* **107**, 923–925 (2007).
3. Gaita-Ariño, A., Luis, F., Hill, S. & Coronado, E. Molecular spins for quantum computation. *Nat. Chem.* **11**, 301–309 (2019).
4. Wasielewski, M. R. et al. Exploiting chemistry and molecular systems for quantum information science. *Nat. Rev. Chem.* **4**, 490–504 (2020).
5. Toninelli, C. et al. Single organic molecules for photonic quantum technologies. *Nat. Mater.* **20**, 1615–1628 (2021).
6. Moreno-Pineda, E. & Wernsdorfer, W. Measuring molecular magnets for quantum technologies. *Nat. Rev. Phys.* **3**, 645–659 (2021).
7. Yu, C.-J., von Kugelgen, S., Laorenza, D. W. & Freedman, D. E. A molecular approach to quantum sensing. *ACS Cent. Sci.* **7**, 712–723 (2021).
8. Utama, M. I. B. et al. Mixed-dimensional heterostructures for quantum photonic science and technology. *MRS Bull.* **48**, 905–913 (2023).
9. Manriquez, J. M., Yee, G. T., McLean, R. S., Epstein, A. J. & Miller, J. S. A room-temperature molecular/organic-based magnet. *Science* **252**, 1415–1417 (1991).
10. Candido, D. R., Fuchs, G. D., Johnston-Halperin, E. & Flatté, M. E. Predicted strong coupling of solid-state spins via a single magnon mode. *Mater. Quantum Technol.* **1**, 011001 (2021).
11. Huebl, H. et al. High cooperativity in coupled microwave resonator ferrimagnetic insulator hybrids. *Phys. Rev. Lett.* **111**, 127003 (2013).
12. Tabuchi, Y. et al. Hybridizing ferromagnetic magnons and microwave photons in the quantum limit. *Phys. Rev. Lett.* **113**, 083603 (2014).
13. Zhang, X., Zou, C.-L., Jiang, L. & Tang, H. X. Strongly coupled magnons and cavity microwave photons. *Phys. Rev. Lett.* **113**, 156401 (2014).
14. Tabuchi, Y. et al. Coherent coupling between a ferromagnetic magnon and a superconducting qubit. *Science* **349**, 405–408 (2015).
15. Lachance-Quirion, D., Tabuchi, Y., Gloppe, A., Usami, K. & Nakamura, Y. Hybrid quantum systems based on magnonics. *Appl. Phys. Express* **12**, 070101 (2019).
16. Clerk, A. A., Lehnert, K. W., Bertet, P., Petta, J. R. & Nakamura, Y. Hybrid quantum systems with circuit quantum electrodynamics. *Nat. Phys.* **16**, 257–267 (2020).
17. Plachy, R. et al. Ferrimagnetic resonance in films of vanadium $[tetracyanoethanide]_x$, grown by chemical vapor deposition. *Phys. Rev. B* **70**, 064411 (2004).
18. Yu, H. et al. Ultra-narrow ferromagnetic resonance in organic-based thin films grown via low temperature chemical vapor deposition. *Appl. Phys. Lett.* **105**, 012407 (2014).
19. Franson, A. et al. Low-damping ferromagnetic resonance in electron-beam patterned, high-Q vanadium tetracyanoethylene magnon cavities. *APL Mater.* **7**, 121113 (2019).
20. Cheung, H. F. H. et al. Raman spectroscopy and aging of the low-loss ferrimagnet vanadium tetracyanoethylene. *J. Phys. Chem. C.* **125**, 20380–20388 (2021).
21. Bola, J. S. et al. Fabrication method, ferromagnetic resonance spectroscopy and spintronics devices based on the organic-based ferrimagnet vanadium tetracyanoethylene. *Adv. Funct. Mater.* **31**, 2100687 (2021).
22. Yusuf, H. et al. Exploring a quantum-information-relevant magnonic material: ultralow damping at low temperature in the organic ferrimagnet $V[TCNE]_x$. *AVS Quantum Sci.* **3**, 026801 (2021).
23. Onbasli, M. C. et al. Pulsed laser deposition of epitaxial yttrium iron garnet films with low Gilbert damping and bulk-like magnetization. *APL Mater.* **2**, 106102 (2014).
24. Pokhodnya, K. I., Epstein, A. J. & Miller, J. S. Thin-film V[TCNE] magnets. *Adv. Mater.* **12**, 410–413 (2000).
25. de Caro, D. et al. CVD-grown thin films of molecule-based magnets. *Chem. Mater.* **12**, 587–589 (2000).
26. Zhu, H. et al. Long-term operating stability in perovskite photovoltaics. *Nat. Rev. Mater.* **8**, 569–586 (2023).
27. Lu, Q. et al. A review on encapsulation technology from organic light emitting diodes to organic and perovskite solar cells. *Adv. Funct. Mater.* **31**, 2100151 (2021).
28. Froning, I. H. et al. Thin-film encapsulation of the air-sensitive organic-based ferrimagnet vanadium tetracyanoethylene. *Appl. Phys. Lett.* **106**, 122403 (2015).
29. Liu, H. et al. Organic-based magnon spintronics. *Nat. Mater.* **17**, 308–312 (2018).
30. Haskel, D. et al. Local structural order in the disordered vanadium tetracyanoethylene room-temperature molecule-based magnet. *Phys. Rev. B* **70**, 054422 (2004).
31. Wood, J. D. et al. Effective passivation of exfoliated black phosphorus transistors against ambient degradation. *Nano Lett.* **14**, 6964–6970 (2014).
32. Wells, S. A. et al. Suppressing ambient degradation of exfoliated InSe nanosheet devices via seeded atomic layer deposition encapsulation. *Nano Lett.* **18**, 7876–7882 (2018).
33. Gish, J. T. et al. Ambient-stable two-dimensional CrI_3 via organic-inorganic encapsulation. *ACS Nano* **15**, 10659–10667 (2021).
34. Pokhodnya, K., Bonner, M., Prigodin, V., Epstein, A. J. & Miller, J. S. Carrier transport in the $V[TCNE]_x$ (TCNE = tetracyanoethylene; $x \sim 2$) organic-based magnet. *J. Phys.: Condens. Matter* **25**, 196001 (2013).
35. Groner, M. D., Fabreguette, F. H., Elam, J. W. & George, S. M. Low-temperature Al_2O_3 atomic layer deposition. *Chem. Mater.* **16**, 639–645 (2004).

36. Oviroh, P. O., Akbarzadeh, R., Pan, D., Coetzee, R. A. M. & Jen, T. C. New development of atomic layer deposition: processes, methods and applications. *Sci. Technol. Adv. Mater.* **20**, 465–496 (2019).
37. Pokhodnya, K. I. & Bonner, M. Parylene protection coatings for thin film V[TCNE]$_x$ room temperature magnets. *Chem. Mater.* **16**, 5114–5119 (2004).
38. Suhl, H. Ferromagnetic resonance in nickel ferrite between one and two kilomegacycles. *Phys. Rev.* **97**, 555–557 (1955).
39. Trout, A. H. et al. Probing the structure of vanadium tetracyanoethylene using electron energy-loss spectroscopy. *APL Mater.* **10**, 081102 (2022).
40. Prigodin, V. N., Raju, N. P., Pokhodnya, K. I., Miller, J. S. & Epstein, A. J. Spin-driven resistance in organic-based magnetic semiconductor V[TCNE]. *Adv. Mater.* **14**, 1230–1233 (2002).
41. Kao, C.-Y., Li, B., Lu, Y., Yoo, J.-W. & Epstein, A. J. Thin films of organic-based magnetic materials of vanadium and cobalt tetracyanoethylene by molecular layer deposition. *J. Mater. Chem. C.* **2**, 6171–6176 (2014).
42. Xu, Q. et al. Strong photon-magnon coupling using a lithographically defined organic ferrimagnet. *Adv. Sci.* **11**, 2310032 (2024).
43. Harberts, M., Lu, Y., Yu, H., Epstein, A. J. & Johnston-Halperin, E. Chemical vapor deposition of an organic magnet, vanadium tetracyanoethylene. *J. Vis. Exp.* **101**, e52891 (2015).
44. Bloch, F. Zur Theorie des Ferromagnetismus. *Z. Phys.* **61**, 206–219 (1930).
45. Probst, S., Song, F. B., Bushev, P. A., Ustinov, A. V. & Weides, M. Efficient and robust analysis of complex scattering data under noise in microwave resonators. *Rev. Sci. Instrum.* **86**, 024706 (2015).

Acknowledgements

This research was primarily supported by the Center for Molecular Quantum Transduction, an Energy Frontier Research Center funded by the U.S. Department of Energy, Office of Science, Office of Basic Energy Sciences, under Award No. DE-SC0021314. This work was performed, in part, at the National Science Foundation Materials Research Science and Engineering Center at Northwestern University under Award No. DMR-2308691. This work made use of the Magnet, Low Temperature and Optics facility (MLTOF), which receives support from the MRSEC Program (NSF DMR-2308691) of the Materials Research Center at Northwestern University. This work also made use of the Keck-II facility (RRID: SCR_026360) of the Northwestern University NUANCE Center, which has received support from the SHyNE Resource (NSF ECCS-2025633), the IIN, and the Northwestern MRSEC program (NSF DMR-2308691). Cavity magnonics measurements were performed using the CMQT low temperature facility at Cornell. In addition, this work made use of facilities at the Cornell NanoScale Facility, an NNCI member supported by the National Science Foundation (NNCI-2025233) and the Cornell Center for Materials Research Shared Facilities, which are supported through the NSF MRSEC program (DMR-1719875). The authors further acknowledge the support of the NanoSystems Laboratory User Facility, which is supported by the Center for Emergent Materials, an NSF MRSEC (DMR-2011876). D.L. acknowledges support from the Swiss National Science Foundation for an Early PostDoc Mobility Fellowship (P2EZP2_181614).

Author contributions

M.I.B.U. conceptualized the experiments from the work initiated by D.L., who developed the ALD encapsulation protocol and performed initial magnetometry measurements. M.I.B.U. performed ALD encapsulation, AFM, magnetometry in PPMS (VSM and broadband FMR), MFM, XPS, UV-vis-NIR, FTIR, ellipsometry, and Raman spectroscopy measurements. R.C. and D.S.C. performed CVD growth of V[TCNE]$_x$ and cavity FMR measurements. S.P. fabricated the microwave resonator and performed the cavity magnonic experiments. S.C. performed first-principles calculations of the electronic transitions. Q.X. assisted in sample loading and setup for the microwave resonator measurements. H.Y.P. and S.D.N. assisted in the characterization of ALD alumina. M.I.B.U., R.C., and S.P. analyzed the data and prepared the manuscript with input from all authors. M.C.H., E.J.H., G.D.F., and G.C.S. supervised the project.

Competing interests

The authors declare no competing interests.

Additional information

Supplementary information The online version contains supplementary material available at https://doi.org/10.1038/s41467-025-65588-0.

Correspondence and requests for materials should be addressed to Gregory D. Fuchs, Ezekiel Johnston-Halperin or Mark C. Hersam.

Peer review information *Nature Communications* thanks Jung-Woo Yoo and the other anonymous reviewer(s) for their contribution to the peer review of this work. A peer review file is available.

Reprints and permissions information is available at http://www.nature.com/reprints

Publisher's note Springer Nature remains neutral with regard to jurisdictional claims in published maps and institutional affiliations.

Open Access This article is licensed under a Creative Commons Attribution-NonCommercial-NoDerivatives 4.0 International License, which permits any non-commercial use, sharing, distribution and reproduction in any medium or format, as long as you give appropriate credit to the original author(s) and the source, provide a link to the Creative Commons licence, and indicate if you modified the licensed material. You do not have permission under this licence to share adapted material derived from this article or parts of it. The images or other third party material in this article are included in the article's Creative Commons licence, unless indicated otherwise in a credit line to the material. If material is not included in the article's Creative Commons licence and your intended use is not permitted by statutory regulation or exceeds the permitted use, you will need to obtain permission directly from the copyright holder. To view a copy of this licence, visit http://creativecommons.org/licenses/by-nc-nd/4.0/.

© The Author(s) 2025